Supporting Information

Electron Delocalization Engineering via Hierarchical Modulation in Single-Atom Catalysts for Highly Efficient Electrochemical CO_2 Reduction

Xu Han,[a,b] Hong Liu,[c]* Pengfei Cao,[d] Weiqiang Tang,[e] Chao Yue Zhang,[b] Martí Biset-Peiró,[b] Ke Xiao,[b] Pengyi Tang,[c] Marc Heggen,[d] Miquel Vega-Paredes,[f] Alba Garzón Manjón,[a] Lirong Zheng,[g]* Rafal E. Dunin-Borkowski,[d] Andreu Cabot,[b,h] Kim Daasbjerg,[i,j] Joan Ramon Morante,[b,k] Ting Zhang,[a,b]* Jordi Arbiol[a,h]*

[a]Catalan Institute of Nanoscience and Nanotechnology (ICN2), CSIC and BIST, Campus UAB, Bellaterra, Barcelona, 08193, Catalonia, Spain

[b]Catalonia Institute for Energy Research (IREC), Jardins de les Dones de Negre 1, Sant Adrià del Besòs, Barcelona, 08930, Catalonia, Spain

[c]State Key Laboratory of Information Functional Materials, 2020 X-Lab, Shanghai Institute of Microsystem and Information Technology, Chinese Academy of Sciences, Shanghai 200050, China

[d]Ernst Ruska-Centre for Microscopy and Spectroscopy with Electrons and Peter Grünberg Institute, Forschungszentrum Jülich GmbH, Jülich, 52425, Germany

[e]State Key Laboratory of Chemical Engineering and School of Chemical Engineering, East China University of Science and Technology, 200237 Shanghai, China

[f]Max-Planck-Institutfur Eisenforschung GmbH (MPIE), 40237, Dusseldorf, Germany

[g]Beijing Synchrotron Radiation Facility, Institute of High Energy Physics, Chinese Academy of Sciences, Beijing, 100049, P. R. China

[h]ICREA, Pg. Lluís Companys 23, Barcelona, 08010, Catalonia, Spain

[i]Department of Chemistry/Interdisciplinary Nanoscience Center (iNANO) Aarhus University Langelandsgade 140, 8000 Aarhus C, Denmark

[j]Novo Nordisk Foundation (NNF) CO_2 Research Center (CORC), Aarhus University, Gustav Wieds Vej 10C, 8000 Aarhus C, Denmark

[k]Department of Physics, Universitat de Barcelona, Barcelona, 08028, Catalonia, Spain

*Correspondence: liuhong01@mail.sim.ac.cn

*Correspondence: zhenglr@ihep.ac.cn

*Correspondence: tingzhang@chem.au.dk

*Correspondence: arbiol@icrea.cat

Materials and Methods

Materials:

If not specified, all chemical reagents were purchased from Sigma-Aldrich. Zinc nitrate hexahydrate ($Zn(NO_3)_2 \cdot 6H_2O$), 2-Aminoterphthalic acid, nickel nitrate hexahydrate ($Ni(NO_3)_2 \cdot 6H_2O$), gold chloride trihydrate ($HAuCl_4$), N,N-dimethylformamide (DMF), ethanol and potassium bicarbonate ($KHCO_3$) were all of analytical grade and used as received without further purification. Meanwhile, all solutions were prepared with Milli-Q water (DI-H_2O, Ricca Chemical, ASTM Type I). The carbon paper and Nafion (N-117 membrane, 0.18 mm thick) membrane were purchased from Alfa Aesar.

Characterization:

The X-ray diffraction (XRD) patterns were obtained by using a Bruker D4 X-ray powder diffractometer using Cu Kα radiation (1.54184 Å). Field emission scanning electron microscopy (FE-SEM) images were collected on a FEI Magellan 400 L scanning electron microscope. High angle annular dark-field (HAADF)-scanning transmission electron microscopy (STEM) images and Energy Dispersive X-Ray Spectroscopy (STEM-EDS) analysis were obtained in an aberration corrected transmission electron microscope FEI Titan G2 80–200 (ChemiSTEM). It is equipped with four EDX detectors and operates at 200 kV. Parts of HAADF-STEM micrographs were acquired in a probe-corrected Titan Themis microscope (Thermo Fisher Scientific) operated at 300 kV by using an HAADF detector and a Tecnai F20 field emission gun microscope with a 0.19 nm point-to-point resolution at 200 kV. Images have been analyzed by using Gatan Digital Micrograph software. X-ray photoelectron

spectroscopy (XPS) was performed on a Phoibos 150 analyser (SPECS GmbH, Berlin, Germany) in ultra-high vacuum conditions (base pressure 4×10^{-10} mbar) with a monochromatic aluminum Kα X-ray source (1486.74 eV). Binding energies (BE) were determined using the C 1s peak at 284.5 eV as a charge reference. Inductively coupled plasma-mass spectrometry (ICP-MS) measurements were carried out to determine the concentration of Ni and Au. Raman spectra were obtained using Senterra. Fourier transformed infrared (FTIR) spectroscopy data were recorded on an Alpha Bruker spectrometer.

XAFS Measurements:

The X-ray absorption fine structure (XAFS) spectra (Fe K-edge) were collected at 1W1B station in Beijing Synchrotron Radiation Facility (BSRF). The storage rings of BSRF were operated at 2.5 GeV with an average current of 250 mA. Using Si(111) double-crystal monochromator, the data collection were carried out in transmission/fluorescence mode using a ionization chamber. All spectra were collected in ambient conditions.

XAFS Analysis and Results:

The acquired EXAFS data were processed according to the standard procedures using the ATHENA module implemented in the IFEFFIT software packages. The k3-weighted EXAFS spectra were obtained by subtracting the post-edge background from the overall absorption and then normalizing with respect to the edge-jump step. Subsequently, k3-weighted $\chi(k)$ data of Fe K-edge were Fourier transformed to real (R) space using a hanning windows (dk=1.0 $Å^{-1}$) to separate the EXAFS contributions from different coordination shells. To obtain quantitative structural parameters around central atoms, least-squares curve parameter fitting was performed using the ARTEMIS module of IFEFFIT software packages.

The k^3 weighting, k-range of 2.4 –11.9 $Å^{-1}$ and R range of 0.95 – 2.25 Å were used for the fitting. The four parameters, coordination number, bond length, Debye-Waller factor and E0 shift (CN, R, σ^2, ΔE^0) were fitted without anyone was fixed, constrained, or correlated. [S1-3]

Ink Preparation in H-cell:

2 mg synthesized different samples and 50 μl 5 wt% Nafion solutions were dissolved in ethanol (500 μL) and ultrasonicated for 1 h to form an evenly suspension for the further electrochemical experiments. To prepare the working electrode, 500 μL above as-prepared inks were dropped onto the two sides of the carbon paper electrode with 1×1 cm^2 and then dried at room temperature, giving a catalyst loading mass of ~1 mg cm^{-2}.

Ink Preparation in Flow-cell:

The catalyst ink was prepared by adding 18 mg $Au_{0.5}$/Ni-N-O-C into a mixed solution of 4 mL isopropanol/water (3:1 (v/v)), and 90 μL Nafion solution (5 wt%), and then was ultrasonically treated for 1 hour to form an evenly suspension for the further electrochemical experiments. To prepare the working electrode, the above as-prepared inks were sprayed onto the gas-diffusion electrode (GDE) with 3×3 cm^2 by air-busher and then dried at room temperature overnight. The final electrode in flow cell was 1×1 cm^2 with a catalyst loading mass of ~1 mg cm^{-2}.

Electrochemical Measurement in H-cell:

The electrocatalytic performance of different catalysts was measured at room temperature by using a gas-tight H-cell with two-compartments separated by Nafion N-117 membrane with a continuous Ar or CO_2 gas injection. Each compartment contained 70 ml electrolyte (0.5 M $KHCO_3$ made from de-ionized water). In a typical experiment, a standard three electrode setup in 0.5 M $KHCO_3$ solution was assembled: an Ag/AgCl electrode as a reference electrode, a Pt plate as a counter electrode and a carbon paper coated with the different samples as a working electrode (surface area = 1 cm^2). The potentials were measured versus Ag/AgCl and converted to the reversible hydrogen electrode (RHE) according to the following equation: $E_{RHE} = E^0_{Ag/AgCl} + E_{Ag/AgCl} + 0.059 \times pH$, pH=7. All electrochemical results were shown without iR-compensation by using a computer-controlled BioLogic VMP3 electrochemical workstation. Meanwhile, the linear sweep voltammetry (LSV) was performed at a scan rate of 20 mV s^{-1} from 0 V to −1.5 V vs. Ag/AgCl in Ar-saturated 0.5 M $KHCO_3$ and CO_2-saturated 0.5 M $KHCO_3$ as supporting electrolyte. The Electrochemical Active Surface Area (ECSA) of different samples was estimated from the electrochemical capacitance measurements. They were tested with scan rates ranging from 2 to 14 mV s^{-1} with an interval of 2 mV s^{-1}. The electrochemical double-layer capacitance (C_{dl}) was estimated by plotting j_a-j_c against the scan rate, where the slope was twice that of C_{dl}. Moreover, electrochemical impedance spectroscopy (EIS) of different samples was carried out in a frequency range from 100 kHz to 100 MHz.

Before the electrochemical CO_2 reduction experiments, an average rate of 20 ml min^{-1}

Ar was injected into cathodic electrolyte to form an Ar-saturated solution. During electrochemical CO_2 reduction experiments, the CO_2 gas was delivered at an average rate of 20 ml min^{-1} at room temperature and ambient pressure, measured downstream by a volumetric digital flowmeter. The gas phase composition was analyzed by gas chromatography (GC) during potentiostatic measurements every 15 min. The calibration of peak area vs. gas concentration was used for the molar quantification of each gaseous effluent. The Faradaic efficiency was calculated by determining the number of coulombs needed for each product and then dividing by the total charge passed during the time of the GC sampling according to the flow rate. Liquid products were analyzed afterwards by quantitative ^{1}H-NMR using water as the deuterated solvent.

Electrochemical Measurement in Flow-cell:

Electrochemical measurements at high current densities were performed in a flow cell using the galvanostatic electrolysis method. GDE coated with catalyst (1.0 cm×1.0 cm), Ag/AgCl (saturated KCl) electrode, and a Ni foam (1.0 cm×1.0 cm) were used as cathode (for CO_2 reduction), reference electrode and anode (for O_2 evolution), respectively. Catholyte and anolyte chambers had an inlet and an outlet for electrolyte, while the CO_2 gas diffusion chamber had an inlet and an outlet for CO_2 gas, and the Ag/AgCl electrode was fixed in the catholyte chamber. Catholyte and anolyte chambers were separated by an anion exchange membrane, anionic exchange membrane and electrolyte chamber for sealing when assembling the flow cell. Catholyte (1 M $KHCO_3$) was circulated in cathode chamber by using a conventional peristaltic pump, while the

anolyte (1 M $KHCO_3$) was circulated through the anode chamber by using a specially made gas-liquid mixed flow pump. CO_2 was delivered to the back of the catholyte chamber at a constant flow 50 sccm by means of a digital mass flow controller.

In-situ **attenuated total reflectance surface-enhanced infrared absorption spectroscopy (ATR-SEIRAS) measurements：**

Surface enhanced infrared absorption spectroscopy (SEIRAS) with an attenuated total reflection (ATR) configuration was employed. A Thermo Nicolet 8700 spectrometer equipped with MCT detector cooled by liquid nitrogen was employed for the electrochemical ATR-SEIRAS measurements. The chemical deposition of the Au thin film (~60 nm) on top of the Si prism was performed according to a "two-step wet process". Before the chemical deposition of Au, the Si prism surface for IR reflection was polished with a Diamond suspension and cleaned in water with sonication. Then the prism was soaked in a piranha solution (7:3 volumetric ratio of 98% H_2SO_4 and 30% H_2O_2) for 2 hours. 30 μL ink was deposited and dried on the Au-film working electrode, then the ink-coated prism was assembled into a homemade spectro-electrochemical cell as the working electrode, Ag/AgCl was used as reference, which was introduced near the working electrode via a Luggin capillary, a Pt mesh (1 cm × 1 cm) was served as the counter electrode. All spectra were shown in $\frac{\Delta R}{R} = \frac{E_S - E_R}{E_R}$, with Es and E_R representing the sample and reference spectra, respectively. The spectral resolution was 4 cm^{-1} for all the measurements if not otherwise mentioned. ATR-SEIRAS was recorded on CO_2-saturated 0.5 M $KHCO_3$ by stepwise switching the potential from −0.40 V to −0.90 V vs. RHE.

Calculation Methods:

Faradaic Efficiency (FE) calculations:

Details concerning the Faradaic Efficiency (FE) calculations are shown below. [S4]

The partial current density for a given gas product was calculated as below:

$$j_i = x_i \times V \times \frac{n_i F P_0}{RT} \times (electrode\ area)^{-1} \quad \text{(eq. S1)}$$

Where x_i is the volume fraction of a certain product determined by online GC referenced to calibration curves from standard gas samples, V is the flow rate, n_i is the number of electrons involved, P_0= 101.3 kPa, F is the Faraday constant, and R is the gas constant. The corresponding FE at each potential is calculated by

$$FE = \frac{j_i}{j} \times 100\% \quad \text{(eq. S2)}$$

TOF calculations:

The TOF was calculated through the following equation:[S4]

$$TOF\ (h^{-1}) = \frac{I_{product}/nF}{\alpha \times m_{cat}/M_{metal}} \times 3600 \quad \text{(eq. S3)}$$

$I_{product}$: partial current density of CO;

n: number of electrons transferred for CO_2 to CO, 2;

F: Faradaic constant, 96485 C/mol;

M_{cat}: catalyst mass in the electrode;

α: mass ratio of active atoms in the catalyst, Ni;

M_{metal}: atomic mass of metal;

DFT Calculations:

Density Functional Theory (DFT) calculations with spin polarization were performed using the Vienna Ab initio Simulation Package (VASP) code,[S5] employing the projector augmented wave (PAW) method.[S6-9] The generalized gradient approximation (GGA), with the Perdew-Burke-Ernzerhof (PBE) exchange-correlation functional was employed to set the plane wave basis. [S10] A 2×2×1 k-point mesh was applied to sample the Brillouin zone for all supercells, with a plane wave cutoff energy of 500 eV. Atomic structure relaxation continued until residual forces were below 0.05 eV/Å. To account for van der Waals interactions between molecules, the DFT-D3 approach was adopted.[S11] Gibbs free energies for individual reaction steps were calculated using the computational hydrogen electrode (CHE) model.[S12] Solvation effects were also considered, stabilizing *CO by 0.1 eV and COOH* by 0.25 eV.[S13] Since the relatively large error in gas-phase CO molecules, we applied a correction of −0.51 eV.[S13] After the correction, the calculated reversible potential for the entire process ($CO_2 + 2H^+ + 2e^- \leftrightarrow CO + H_2O$) is −0.07 V vs. RHE, which is in close agreement with the experimental value of −0.1 V vs. RHE. A vacuum thickness of over 12 Å was applied to ensure adequate separation between the slab and its periodic images along the normal direction. The optimized structural model is shown in **Figure S29**. For the electrochemical CO_2 reduction reaction (eCO_2RR), the following elementary steps were considered:

$$CO_2(g) + * + H^+(aq) + e^- \leftrightarrow *COOH \quad \text{(eq. S4)}$$

$$*COOH + H^+(aq) + e^- \leftrightarrow *CO + H_2O(l) \quad \text{(eq. S5)}$$

$$*CO \leftrightarrow CO(g) + * \quad \text{(eq. S6)}$$

Here, (g), *, and (aq) represent the gaseous phase, adsorption state, and aqueous phase, respectively. The free energies of each species were calculated using the following formula:

$$G = E_{DFT} + E_{ZPE} + \int C_p dT - TS \quad \text{(eq. S7)}$$

where E_{DFT} represents the total energy calculated by DFT, E_{ZPE} is the zero-point energy, C_p is the heat capacity and S is the entropy. The latter three terms are calculated from vibrational frequencies within the ideal-gas limit and harmonic limit at 298.15 K for gas molecules and adsorbates, respectively.[S14] The corresponding values are provided in **Table S4** and **Table S5**.

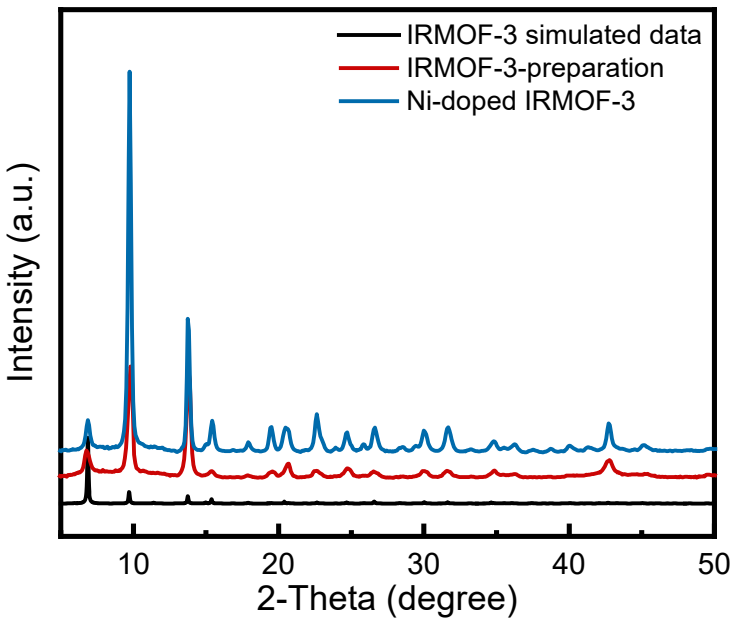

Figure S1. XRD patterns of IRMOF-3 and Ni-IRMOF-3.

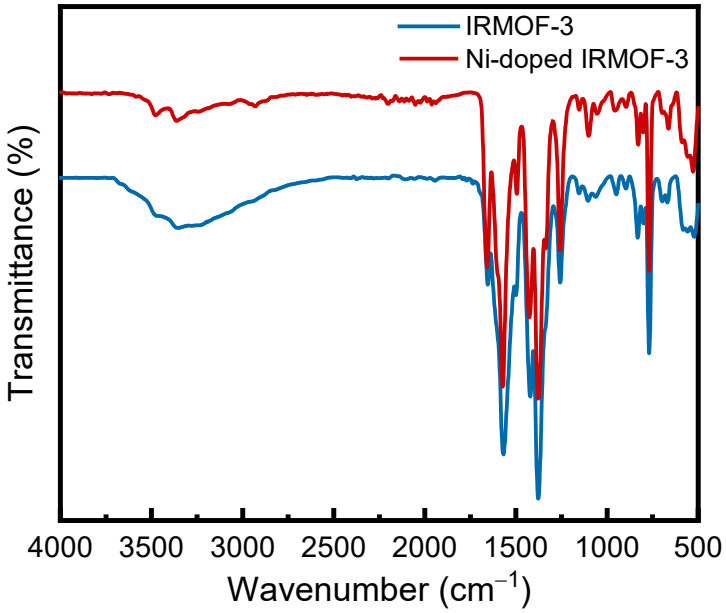

Figure S2. FTIR spectra for IRMOF-3 and Ni-IRMOF-3 samples.

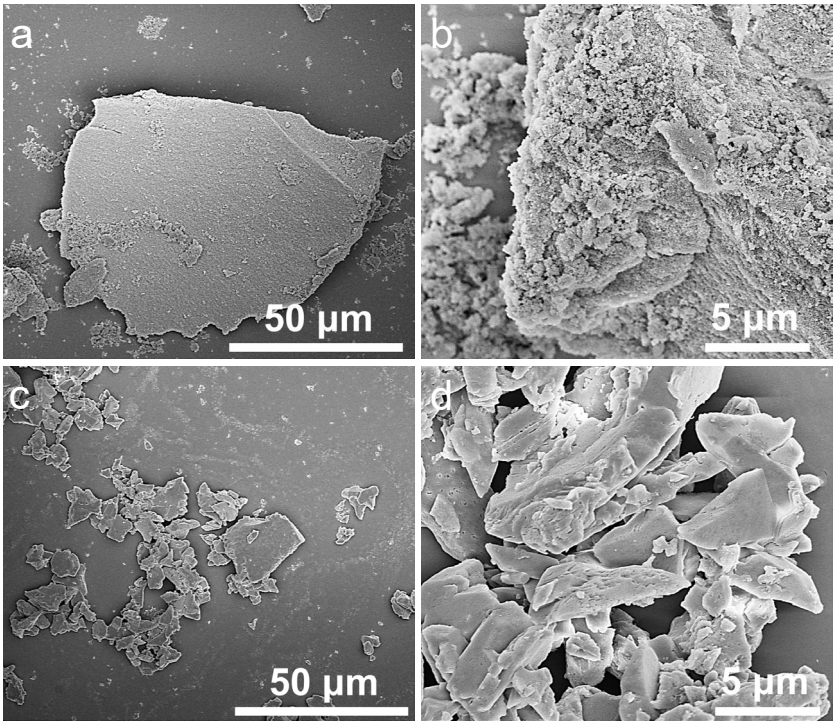

Figure S3. SEM images of (a, b) IRMOF-3 and (c, d) Ni-IRMOF-3.

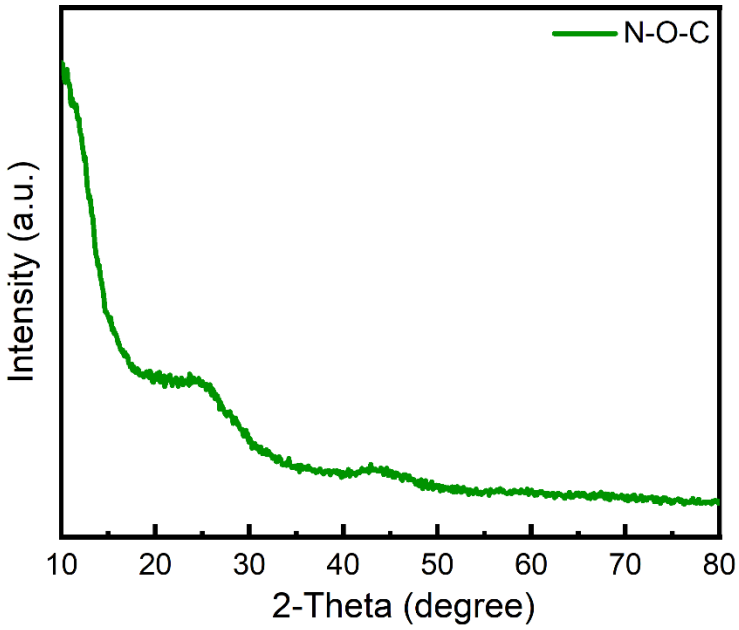

Figure S4. XRD patterns for N-O-C.

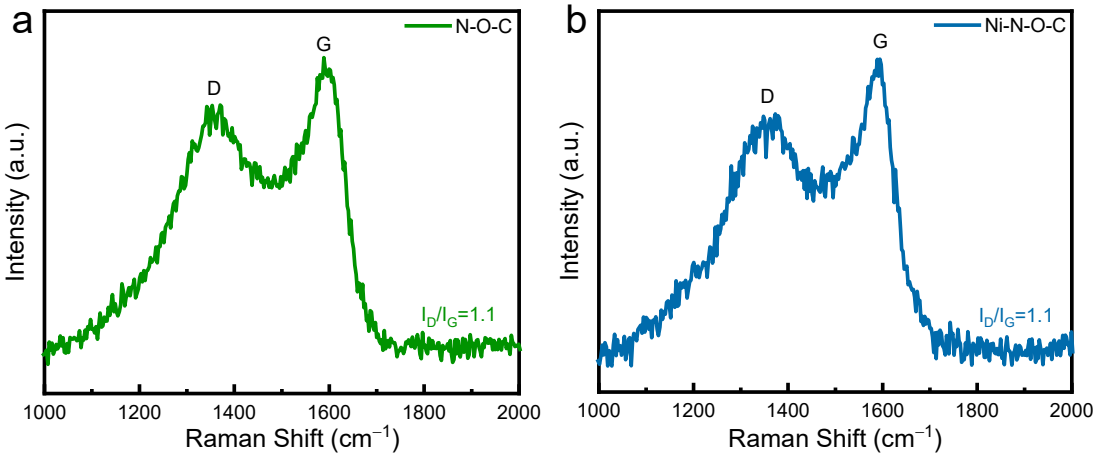

Figure S5. Raman spectra for (a) N-O-C and (b) Ni-N-O-C.

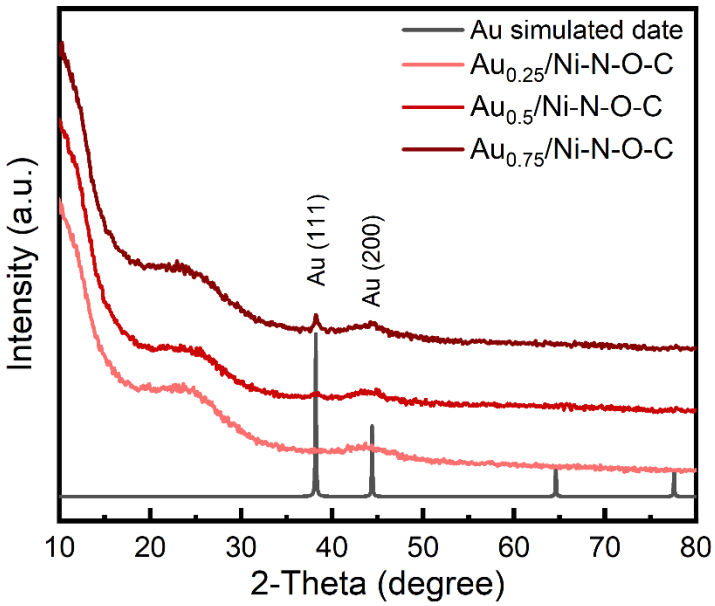

Figure S6. XRD patterns for Au_x/Ni-N-O-C.

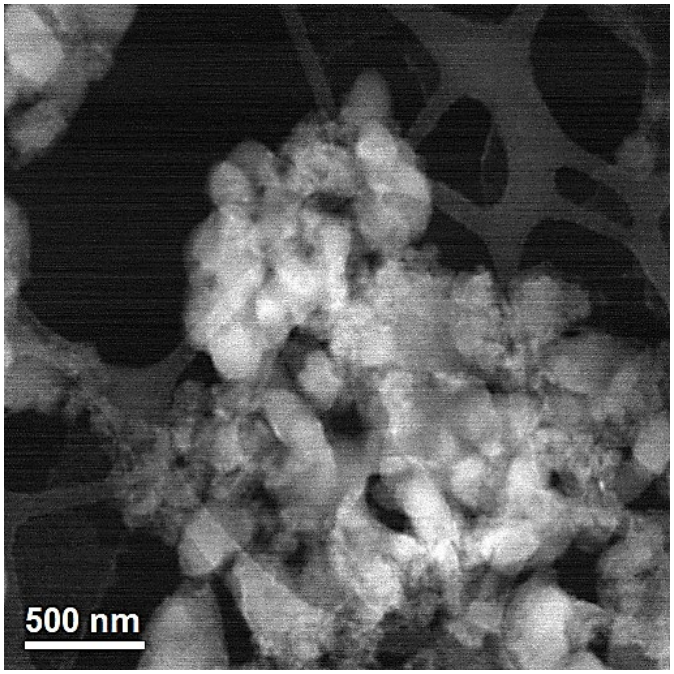

Figure S7. Low-magnification HAADF STEM images of N-O-C.

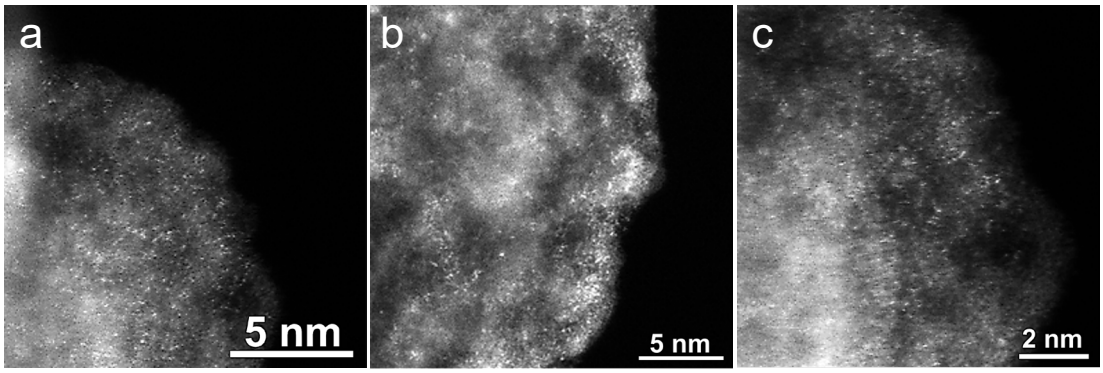

Figure S8. (a-c) High magnification aberration-corrected HAADF STEM images of Ni-N-O-C sample.

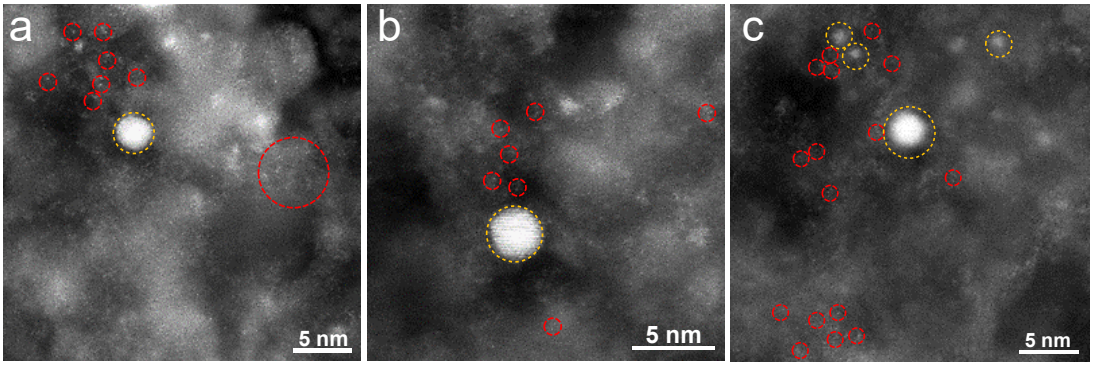

Figure S9. (a-c) High magnification aberration-corrected HAADF STEM images of $Au_{0.5}$/Ni-N-O-C sample.

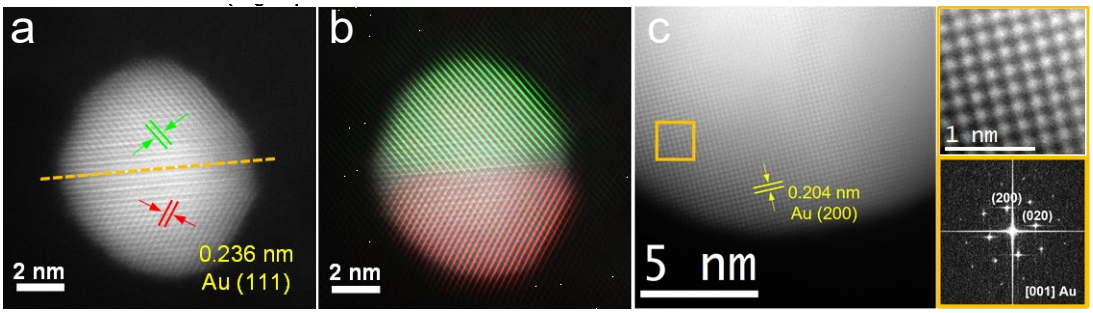

Figure S10. (a) AC HAADF-STEM image of one of the Au nanoparticles in $Au_{0.5}$/Ni-N-O-C sample. The twin boundary in the middle (marked with an orange dashed line) divides the core into two semi spheres. (b) shows the colored twinned (111) planes in the upper (green) and bottom (red) hemispheres in the frequency filtered map of (a). (c) AC HAADF-STEM image of one of the Au nanoparticles with a magnified detail and its corresponding indexed power spectrum.

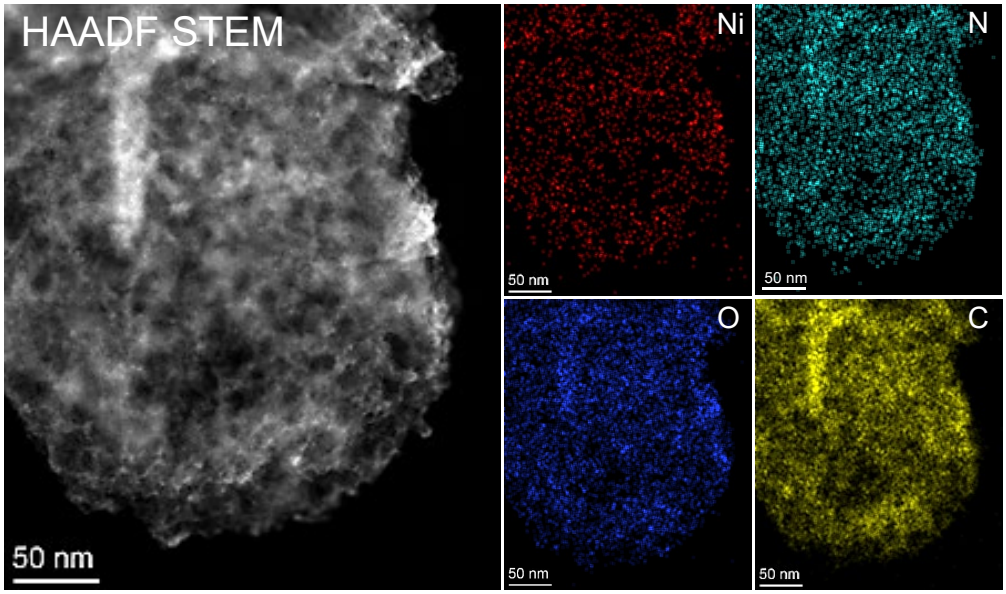

Figure S11. HAADF STEM image of Ni-N-O-C and representative EDS chemical composition maps.

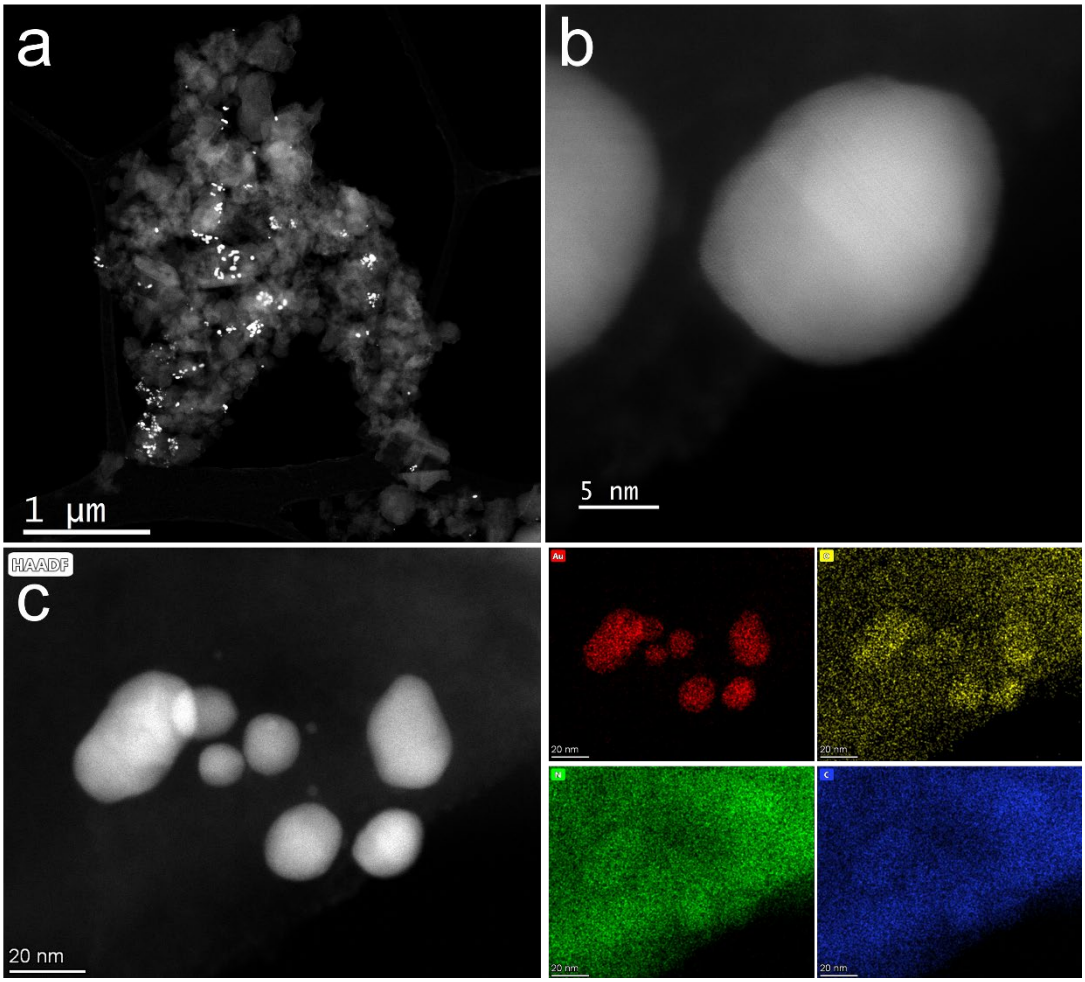

Figure S12. (a) Low magnification and (b) high magnification aberration-corrected HAADF STEM images of $Au_{0.5}$/N-O-C sample, (c) HAADF STEM image and representative EDS chemical compositions of $Au_{0.5}$/N-O-C sample.

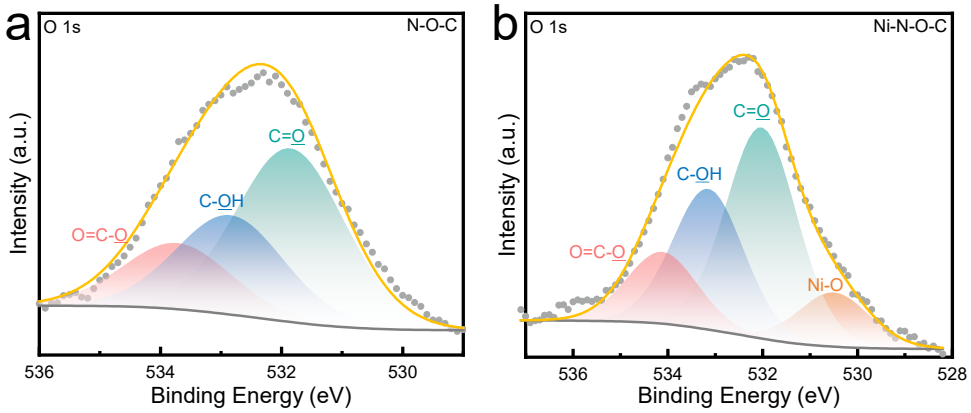

Figure S13. High-resolution XPS O 1s of (a) N-O-C and (b) Ni-N-O-C.

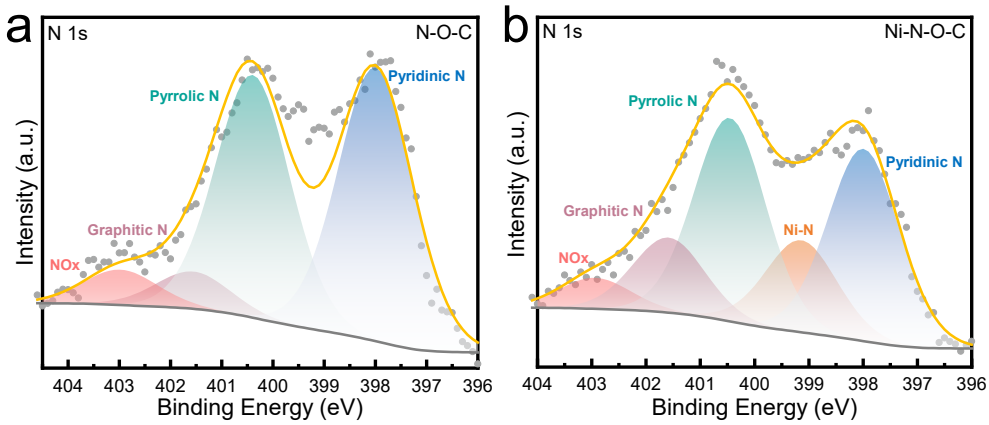

Figure S14. High-resolution XPS N 1s of (a) N-O-C and (b) Ni-N-O-C.

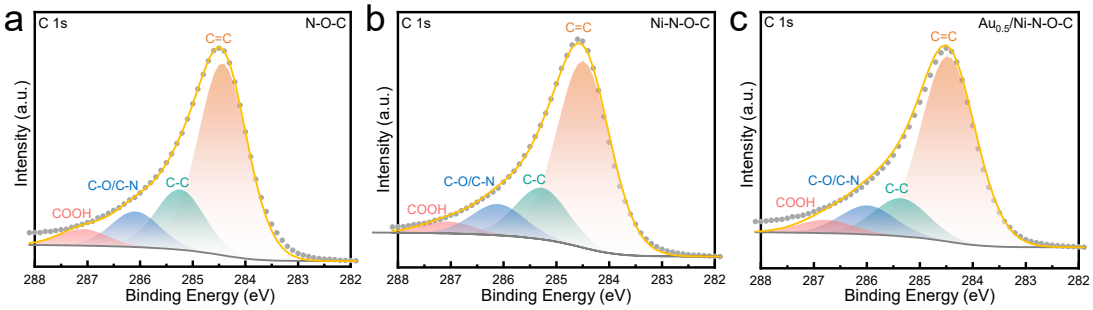

Figure S15. High-resolution XPS C 1s of (a) N-O-C, (b) Ni-N-O-C and (c) $Au_{0.5}$/Ni-N-O-C.

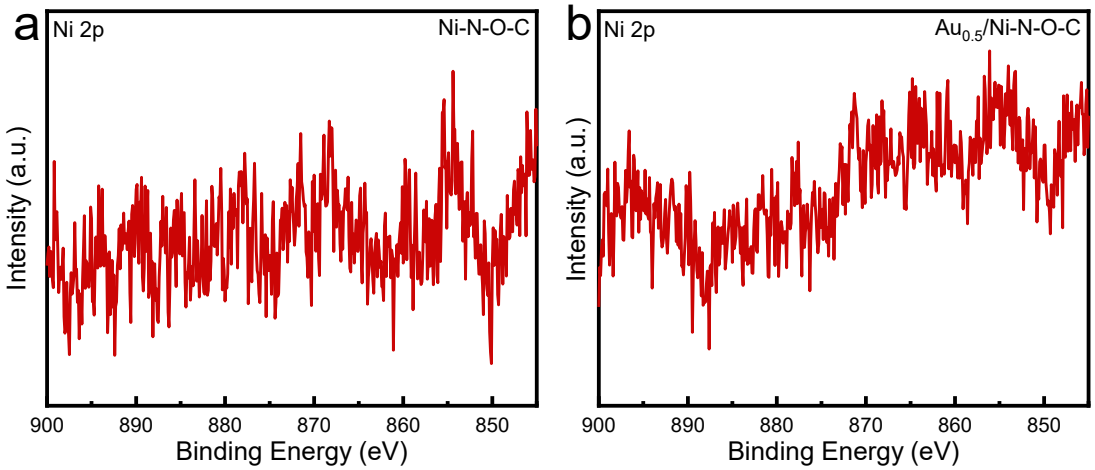

Figure S16. High-resolution XPS Ni 2p of (a) Ni-N-O-C and (b) $Au_{0.5}$/Ni-N-O-C.

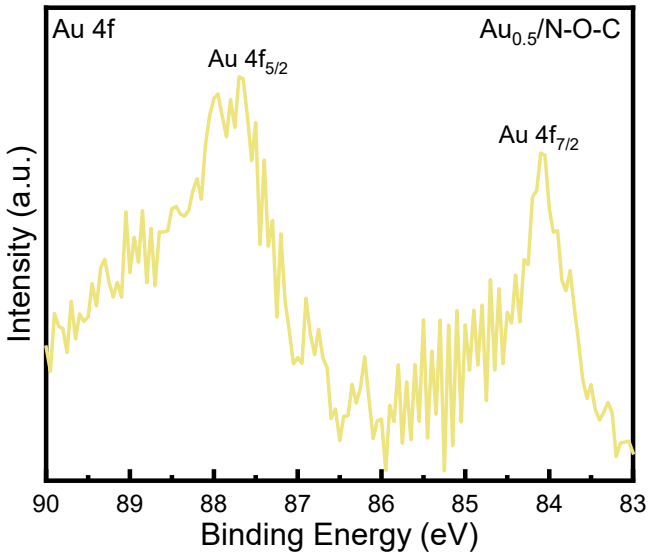

Figure S17. High-resolution XPS Au 4f spectrum of $Au_{0.5}$/N-O-C.

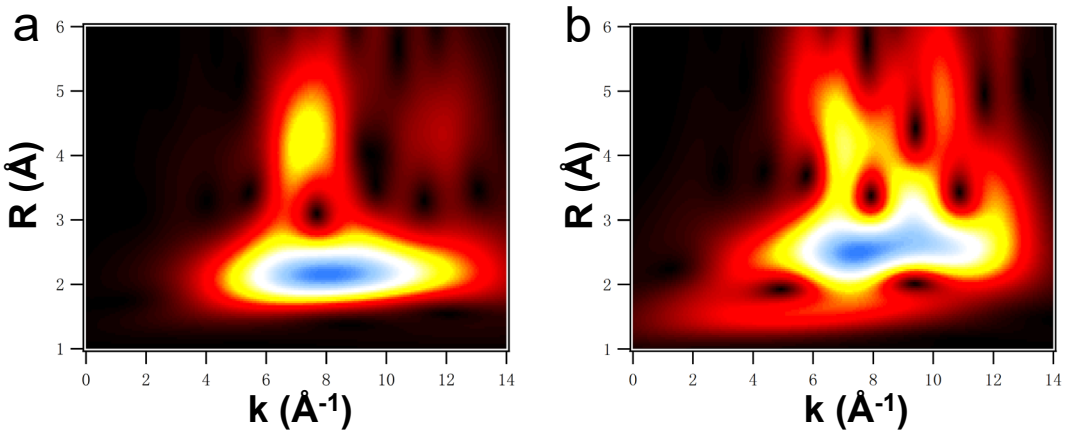

Figure S18. WT-EXAFS images of (a) Ni foil and (b) NiO.

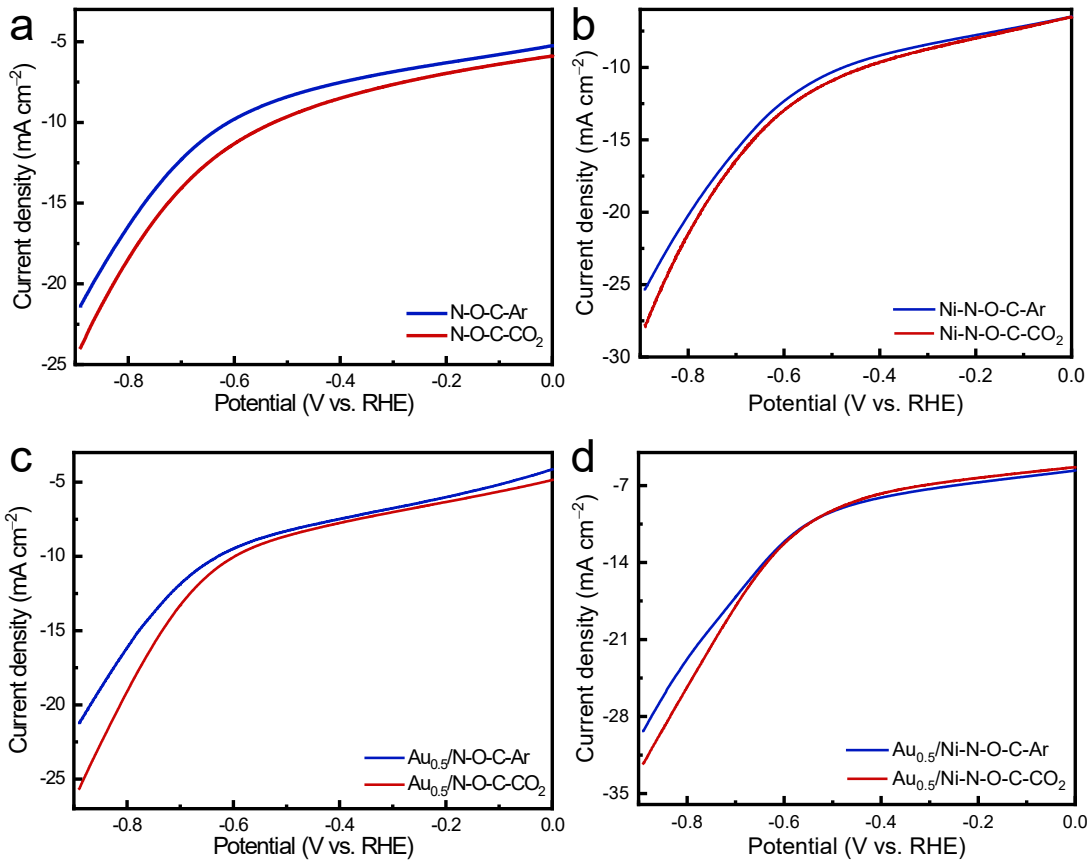

Figure S19. LSV curves vs. RHE of (a) N-O-C, (b) Ni-N-O-C, (c) $Au_{0.5}$/N-O-C and (d) $Au_{0.5}$/Ni-N-O-C obtained in Ar- or CO_2-saturated 0.5 M $KHCO_3$ solution.

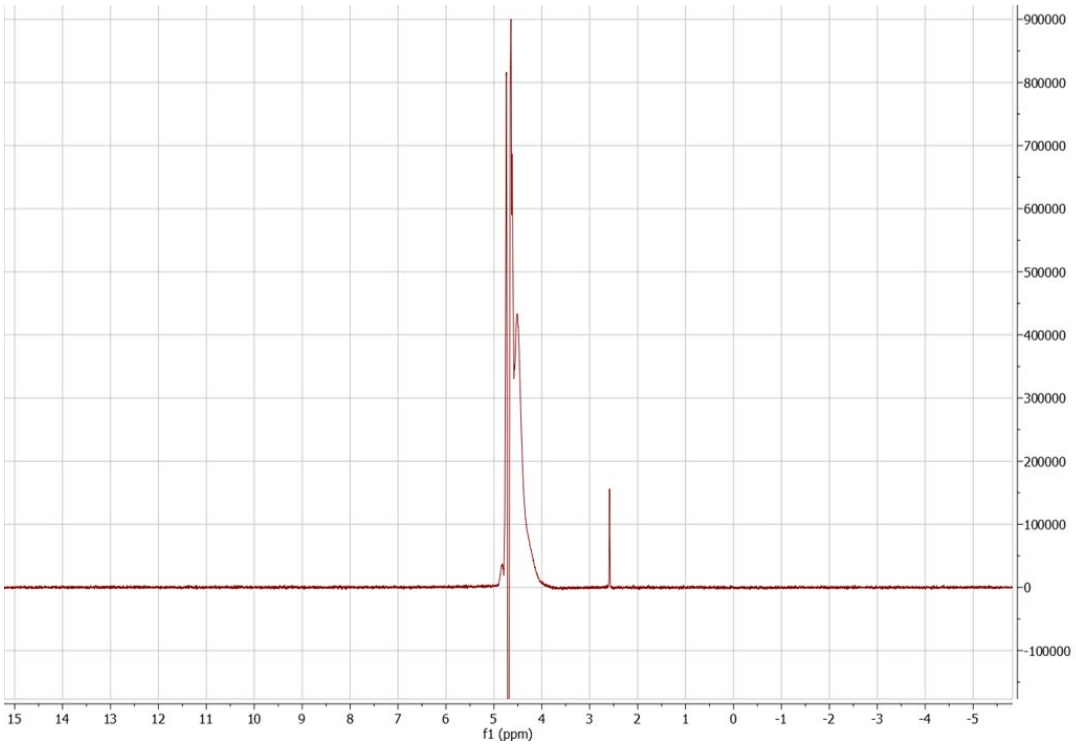

Figure S20. The representative ^{1}H-NMR spectra of the electrolyte after electrolysis of −0.50 V vs. RHE for $Au_{0.5}$/Ni-N-O-C in CO_2-saturated 0.5 M $KHCO_3$ electrolyte for 30 h.

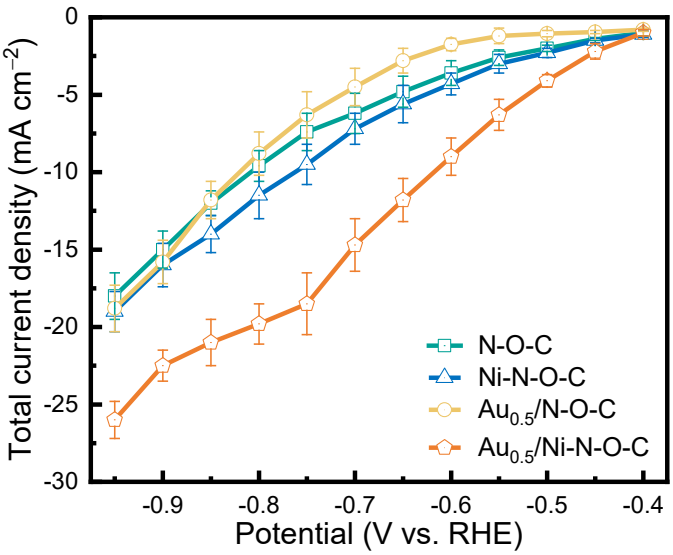

Figure S21. Total current density for different catalysts.

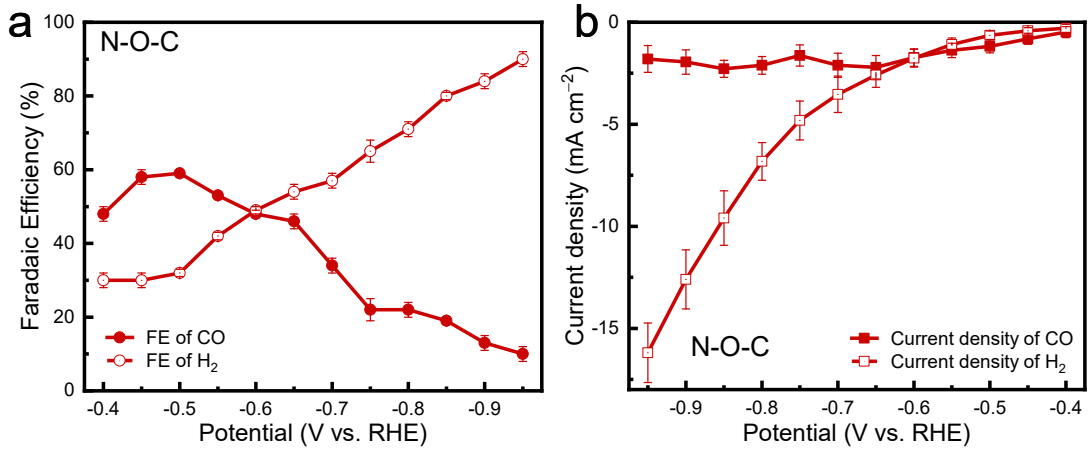

Figure S22. (a) FE of CO and H_2 at various potentials, (b) current density for CO and H_2 on N-O-C.

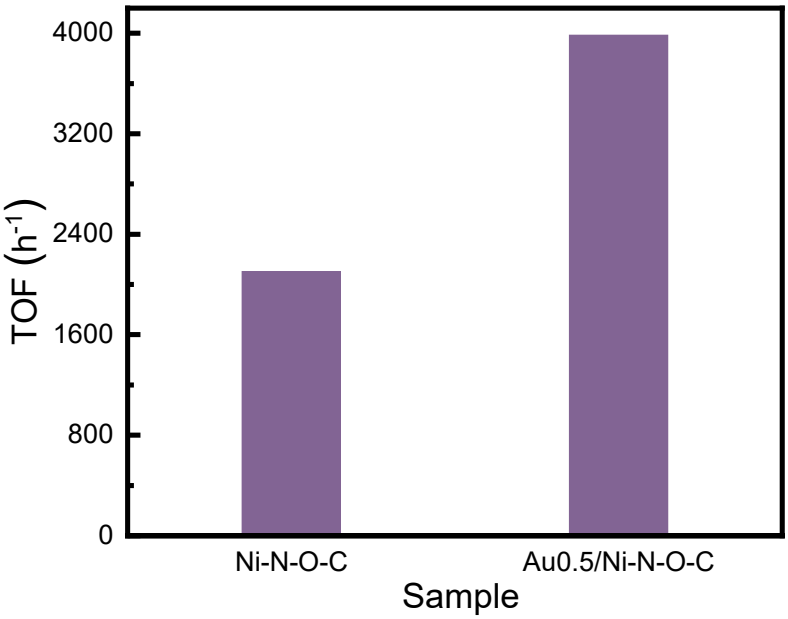

Figure S23. TOF value of Ni-N-O-C and $Au_{0.5}$/Ni-N-O-C.

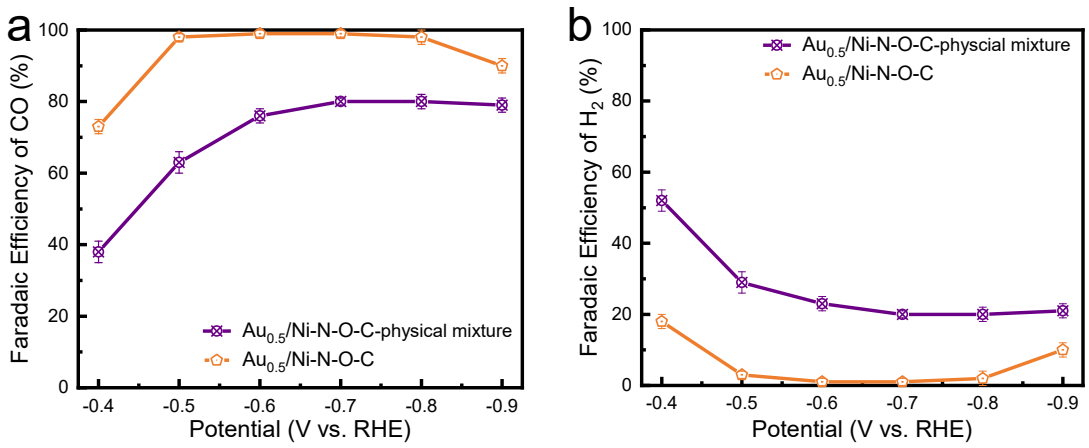

Figure S24. (a) FE of CO and (b) FE of H_2 at various potentials on $Au_{0.5}$/Ni-N-O-C and $Au_{0.5}$/Ni-N-O-C-physical mixture samples.

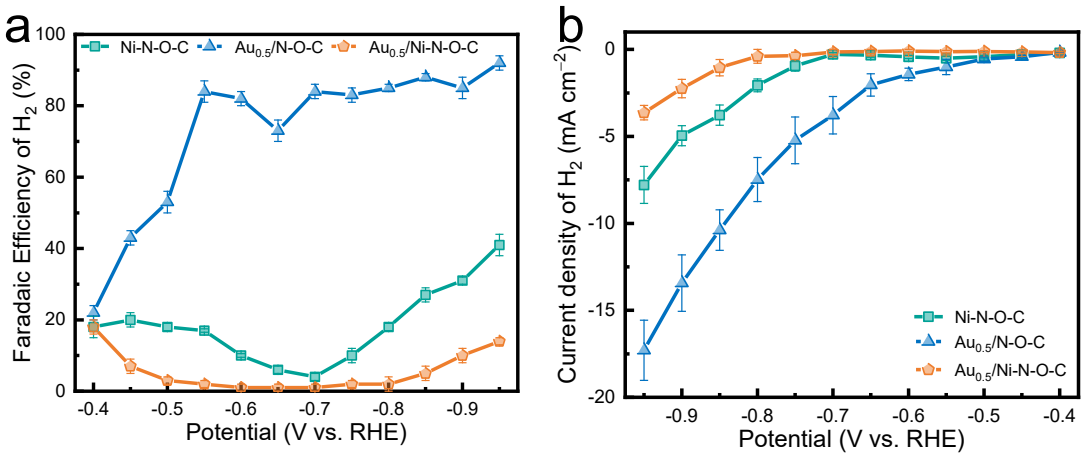

Figure S25. (a) Faradaic efficiency of H_2 and (b) current density for H_2 production on Ni-N-O-C, $Au_{0.5}$/N-O-C and $Au_{0.5}$/Ni-N-O-C samples.

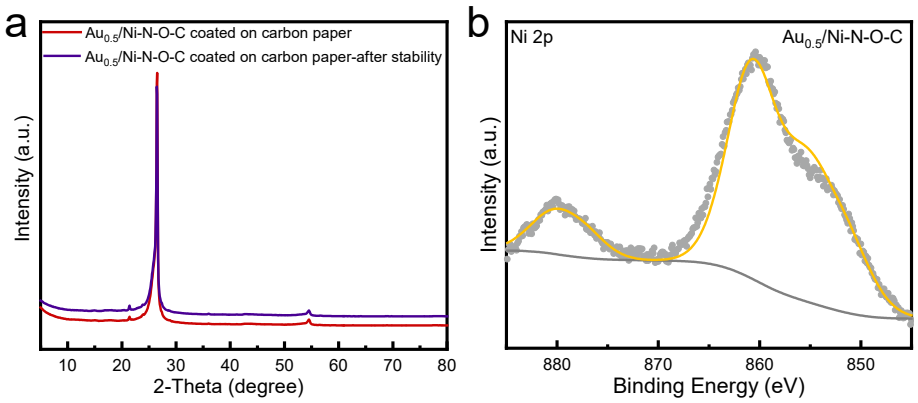

Figure S26. (a) XRD patterns and High-resolution XPS Ni 2p of $Au_{0.5}$/Ni-N-O-C and $Au_{0.5}$/Ni-N-O-C after stability test.

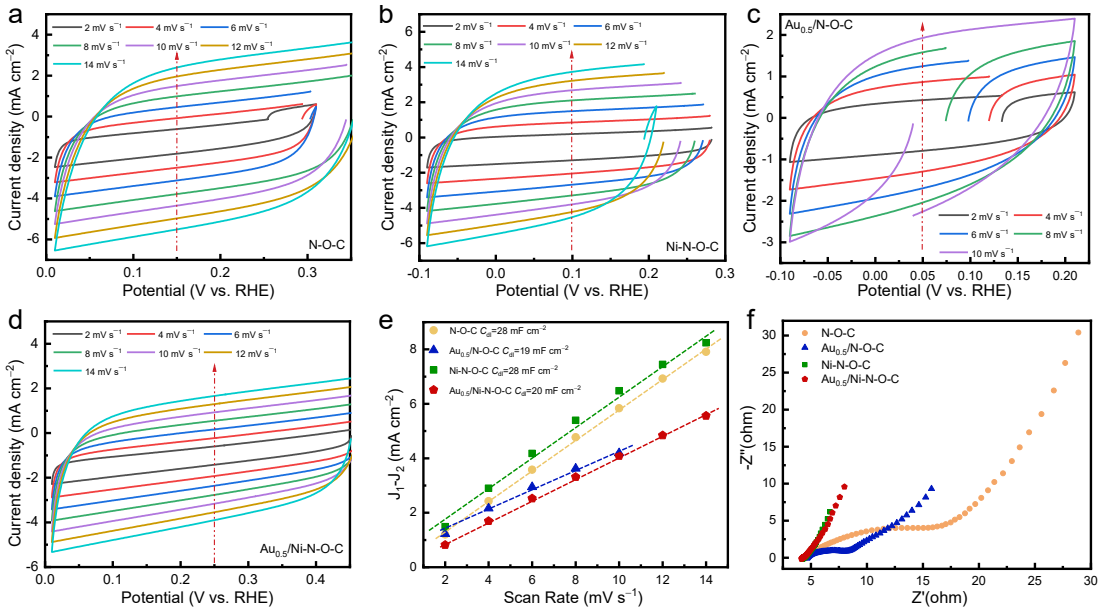

Figure S27. Cyclic voltammograms curves for (a) N-O-C, (b) Ni-N-O-C, (c) $Au_{0.5}$/N-O-C, (d) $Au_{0.5}$/Ni-N-O-C. (e) Plots of the current density vs. scan rate for N-O-C, Ni-N-O-C, $Au_{0.5}$/N-O-C and $Au_{0.5}$/Ni-N-O-C electrodes. (f) Electrochemical impedance spectroscopy (EIS) of N-O-C, Ni-N-O-C, $Au_{0.5}$/N-O-C and $Au_{0.5}$/Ni-N-O-C electrodes.

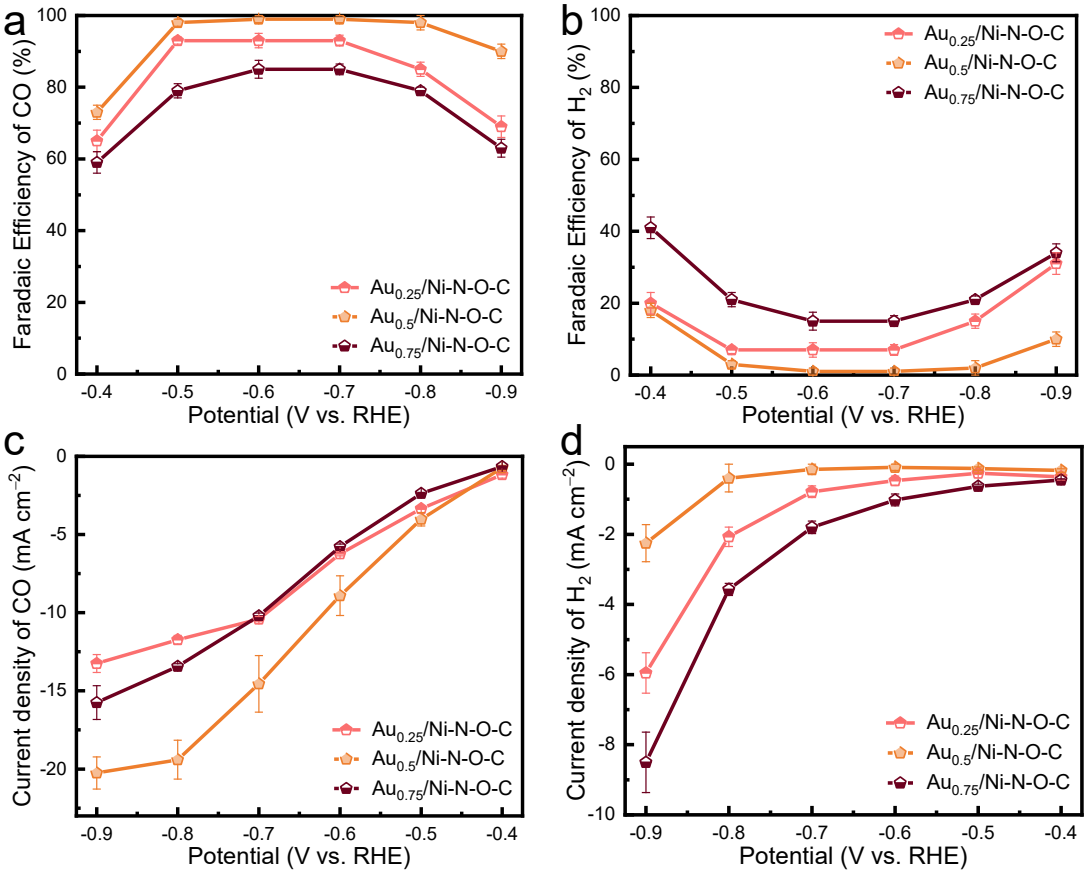

Figure S28. FE of (a) CO and (b) H_2 at various potentials, current density for (c) CO and (d) H_2 production on Au_x/Ni-N-O-C samples.

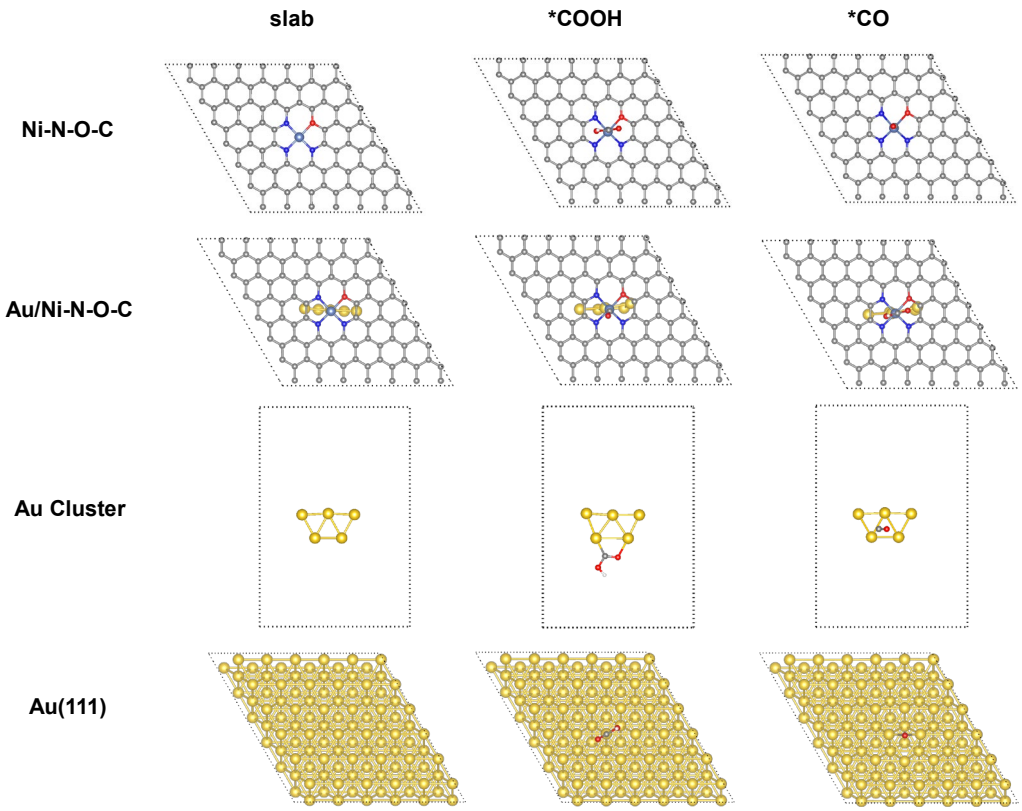

Figure S29. The top view of optimized adsorption configuration on simulated models (Ni, O, N, C and Au atoms are represented in purple, red, blue, grey and gold, respectively).

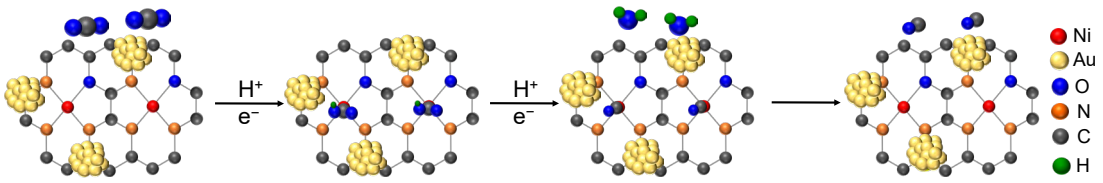

Figure S30. Supposed pathway of CO_2 reduction to CO in DFT calculations.

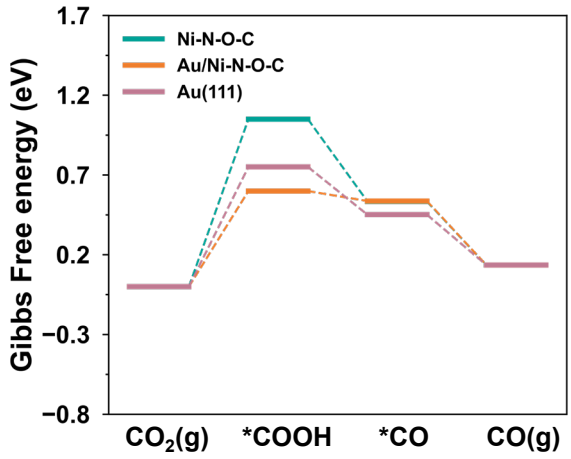

Figure S31. Free energy profiles for the eCO_2RR to CO on simulated models.

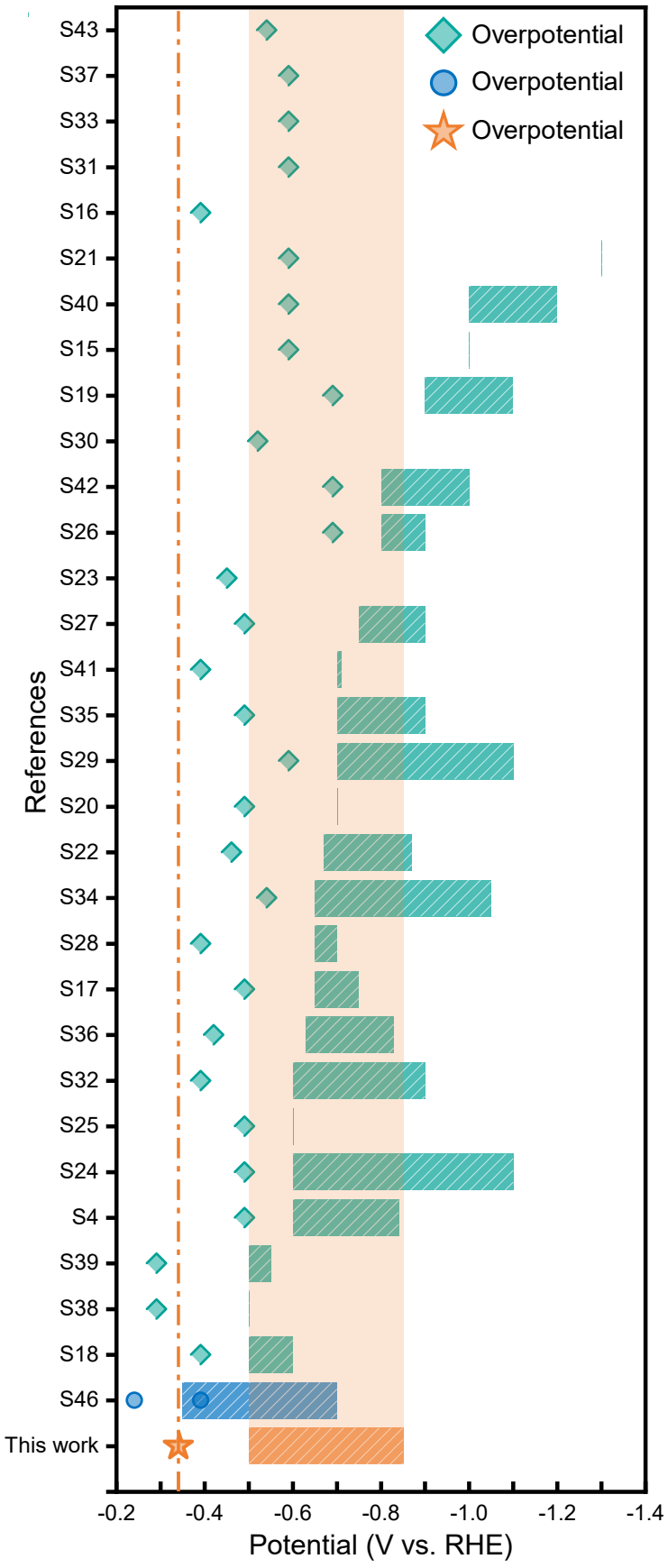

Figure S32. Potential ranges and overpotential of $Au_{0.5}$/Ni-N-O-C (orange) catalyst compared with the state-of-the-art CO_2-to-CO conversion on Ni (green) or Au (blue)-based catalysts.

Table S1. Ni and Au loading ratios of different samples.

Samples	Final product ratio (Ni)	Final product ratio (Au)
Ni-N-O-C	0.18 wt%	/
$Au_{0.5}$/Ni-N-O-C	0.20 wt%	0.38 wt%

Table S2. EXAFS fitting parameters at the Ni K-edge for Ni-N-O-C

Sample	Shell	N [a]	R (Å) [b]	σ^2 (Å^2·10^{-3}) [c]	ΔE0 (eV) [d]	*R* factor (%)
Ni-N-O-C	Ni-N	2.9	1.87	5.7	6.5	0.4
	Ni-O	1.2	2.12	8.4		

[a] *N*: coordination numbers; [b] *R*: bond distance; [c] σ^2: Debye-Waller factors; [d] ΔE_0: the inner potential correction. *R* factor: goodness of fit. *S*02 were set as 0.85/0.80 for Ru-N/O, Ru-Ru, which was obtained from the experimental EXAFS fit of reference NiPc by fixing CN as the known crystallographic value and was fixed to all the samples.

Table 3. Faradaic Efficiency (CO) of the reported Ni or Au-based catalysts for CO_2 electroreduction.

Catalysts	Overpotential @ FE_{CO} > 90% / mV	Potential range (FE_{CO} > 95%)	Reference
NiN_x	490	−0.60 to −0.84 V vs. RHE	[S4]
$NiC_4/NiNC_2$	590	/	[S15]
NiN_4	390	/	[S16]
NiN_2	490	−0.65 to −0.75 V vs. RHE	[S17]
NiN_4-$S_{substrate}$	390	−0.50 to −0.60 V vs. RHE	[S18]
NiN_3	690	−0.90 to −1.10 V vs. RHE	[S19]
NiN_4	490	/	[S20]
NiN_4	590	/	[S21]
NiN_4O_{axial}	460	−0.67 to −0.87 V vs. RHE	[S22]
NiN_4O_{axial}	450	/	[S23]
$NiN_4B_{substrate}$	490	−0.60 to −1.10 V vs. RHE	[S24]
NiN_4	490	/	[S25]
NiN_3	690	−0.80 to −0.90 V vs. RHE	[S26]
NiN_4	490	−0.75 to −0.90 V vs. RHE	[S27]
NiN_4	390	−0.65 to −0.70 V vs. RHE	[S28]
NiN_4	590	−0.70 to −1.10 V vs. RHE	[S29]
NiN_4	520	/	[S30]
NiN_2C_2	590	/	[S31]
NiN_4	390	−0.60 to −0.90 V vs. RHE	[S32]
NiN_3S	590	/	[S33]
NiN_3B	540	−0.65 to −1.05 V vs. RHE	[S34]
NiN_2	490	−0.70 to −0.90 V vs. RHE	[S35]
NiN_3S	420	−0.63 to −0.83 V vs. RHE	[S36]
Ni/Fe-N-C	590	/	[S37]
Ni/Fe-N-C	290	/	[S38]
Ni/Fe-N-C	290	−0.50 to −0.55 V vs. RHE	[S39]
Ni/Cu-N-C	590	−1.00 to −1.20 V vs. RHE	[S40]
Ni/In-N-C	390	/	[S41]
Ni/Ni-N-C	690	−0.80 to −1.00 V vs. RHE	[S42]
Ni-N-C	540	/	[S43]
Ni-N-C	690	/	[S44]
Au needles	240	−0.35 to −0.50 V vs. RHE	[S45]
Au particles	390	−0.50 to −0.70 V vs. RHE	[S46]
$Au_{0.5}/NiN_3O$	340	**−0.50 V to –0.85 V** vs. RHE	**This work**

Table S4. Thermodynamic free energy corrections (in eV) for gas molecules.

Species	E_{ZPE} (eV)	$\int C_p dT$ (eV)	TS (eV)
CO(g)	0.13	0.09	0.61
CO_2(g)	0.31	0.10	0.66
H_2(g)	0.27	0.09	0.40
H_2O(g=l)	0.57	0.10	0.67

Table S5. Thermodynamic free energy corrections (in eV) for adsorbates.

Models	Adsorbates	E_{ZPE} (eV)	$\int C_p dT$ (eV)	TS (eV)
Ni-N-O-C	COOH*	0.60	0.11	0.26
	CO*	0.19	0.05	0.12
Au Cluster	COOH*	0.63	0.10	0.19
	CO*	0.14	0.07	0.18
Au/Ni-N-O-C	COOH*	0.62	0.11	0.23
	CO*	0.19	0.08	0.19
Au(111)	COOH*	0.61	0.09	0.19
	CO*	0.18	0.08	0.15

References

[1] B. Ravel, M. Newville, ATHENA, ARTEMIS, HEPHAESTUS: data analysis for X-ray absorption spectroscopy using IFEFFIT, J. Synchrotron Radiat. 12(4) (2005) 537-541. https://doi.org/doi:10.1107/S0909049505012719.

[2] D.D. Koningsberger, R. Prins, X-ray absorption : principles, applications, techniques of EXAFS, SEXAFS and XANES, Chem. Anal. (Warsaw) 92 (1988).

[3] J.J. Rehr, R.C. Albers, Theoretical approaches to x-ray absorption fine structure, Rev. Modern Phys. 72(3) (2000) 621-654. https://doi.org/10.1103/RevModPhys.72.621.

[4] T. Zheng, K. Jiang, N. Ta, Y. Hu, J. Zeng, J. Liu, H. Wang, Large-Scale and Highly Selective CO2 Electrocatalytic Reduction on Nickel Single-Atom Catalyst, Joule 3(1) (2019) 265-278. https://doi.org/https://doi.org/10.1016/j.joule.2018.10.015.

[5] J. Hafner, Ab-Initio Simulations of Materials Using VASP: Density-Functional Theory and Beyond, J. Comput. Chem. 29(13) (2008) 2044.

[6] P.E. Blöchl, Projector augmented-wave method, Phys. Rev. B 50(24) (1994) 17953-17979. https://doi.org/10.1103/PhysRevB.50.17953.

[7] G. Kresse, J. Furthmüller, Efficient Iterative Schemes for ab Initio Total-Energy Calculations Using a Plane-Wave Basis Set, Phys. Rev. B 54(16) (1996) 11169-11186.

[8] G. Kresse, J. Furthmüller, Efficiency of ab-initio total energy calculations for metals and semiconductors using a plane-wave basis set, Comput. Mater. Sci. 6(1) (1996) 15-50. https://doi.org/https://doi.org/10.1016/0927-0256(96)00008-0.

[9] G. Kresse, D. Joubert, From Ultrasoft Pseudopotentials to the Projector Augmented-Wave Method, Phys. Rev. B 59(3) (1999) 1758-1775.

[10] J.P. Perdew, K. Burke, M. Ernzerhof, Generalized Gradient Approximation Made Simple, Phys. Rev. Lett. 77(18) (1996) 3865-3868.

[11] S. Grimme, J. Antony, S. Ehrlich, H. Krieg, A consistent and accurate ab initio parametrization of density functional dispersion correction (DFT-D) for the 94 elements H-Pu, J. Chem. Phys. 132(15) (2010) 154104. https://doi.org/10.1063/1.3382344.

[12] J.K. Nørskov, J. Rossmeisl, A. Logadottir, L. Lindqvist, J.R. Kitchin, T. Bligaard, H. Jónsson, Origin of the Overpotential for Oxygen Reduction at a Fuel-Cell Cathode, J. Phys. Chem. B 108(46) (2004) 17886-17892. https://doi.org/10.1021/jp047349j.

[13] A.A. Peterson, F. Abild-Pedersen, F. Studt, J. Rossmeisl, J.K. Norskov, How Copper Catalyzes the Electroreduction of Carbon Dioxide into Hydrocarbon Fuels, Energy Environ. Sci. 3(9) (2010) 1311-1315. https://doi.org/10.1039/C0EE00071J.

[14] Y. Wang, P. Hou, Z. Wang, P. Kang, Zinc Imidazolate Metal–Organic Frameworks (ZIF-8) for Electrochemical Reduction of CO_2 to CO, ChemPhysChem 18(22) (2017) 3142-3147. https://doi.org/https://doi.org/10.1002/cphc.201700716.

[15] C. Zhao, Y. Wang, Z. Li, W. Chen, Q. Xu, D. He, D. Xi, Q. Zhang, T. Yuan, Y. Qu, J. Yang, F. Zhou, Z. Yang, X. Wang, J. Wang, J. Luo, Y. Li, H. Duan, Y. Wu, Y. Li, Solid-Diffusion Synthesis of Single-Atom Catalysts Directly from Bulk Metal for Efficient CO_2 Reduction, Joule 3(2) (2019) 584-594. https://doi.org/https://doi.org/10.1016/j.joule.2018.11.008.

[16] Y. Li, N.M. Adli, W. Shan, M. Wang, M.J. Zachman, S. Hwang, H. Tabassum, S. Karakalos, Z. Feng, G. Wang, Y.C. Li, G. Wu, Atomically dispersed single Ni site catalysts for high-efficiency CO_2 electroreduction at industrial-level current densities, Energy Environ. Sci. 15(5) (2022) 2108-2119. https://doi.org/10.1039/D2EE00318J.

[17] Y. Zhou, Q. Zhou, H. Liu, W. Xu, Z. Wang, S. Qiao, H. Ding, D. Chen, J. Zhu, Z. Qi, X. Wu, Q. He, L. Song, Asymmetric dinitrogen-coordinated nickel single-atomic sites for efficient CO_2 electroreduction, Nat. Commun. 14(1) (2023) 3776. https://doi.org/10.1038/s41467-023-39505-2.
[18] H.B. Yang, S.-F. Hung, S. Liu, K. Yuan, S. Miao, L. Zhang, X. Huang, H.-Y. Wang, W. Cai, R. Chen, J. Gao, X. Yang, W. Chen, Y. Huang, H.M. Chen, C.M. Li, T. Zhang, B. Liu, Atomically dispersed Ni(i) as the active site for electrochemical CO_2 reduction, Nat. Energy 3(2) (2018) 140-147. https://doi.org/10.1038/s41560-017-0078-8.
[19] W. Hua, H. Sun, L. Lin, Q. Mu, B. Yang, Y. Su, H. Wu, F. Lyu, J. Zhong, Z. Deng, Y. Peng, A hierarchical Single-Atom Ni-N3-C catalyst for electrochemical CO_2 reduction to CO with Near-Unity faradaic efficiency in a broad potential range, Chem. Eng. J. 446 (2022) 137296. https://doi.org/https://doi.org/10.1016/j.cej.2022.137296.
[20] R. Boppella, M. Austeria P, Y. Kim, E. Kim, I. Song, Y. Eom, D.P. Kumar, M. Balamurugan, E. Sim, D.H. Kim, T.K. Kim, Pyrrolic N-Stabilized Monovalent Ni Single-Atom Electrocatalyst for Efficient CO_2 Reduction: Identifying the Role of Pyrrolic–N and Synergistic Electrocatalysis, Adv. Funct. Mater. 32(35) (2022) 2202351. https://doi.org/https://doi.org/10.1002/adfm.202202351.
[21] D. Xi, J. Li, J. Low, K. Mao, R. Long, J. Li, Z. Dai, T. Shao, Y. Zhong, Y. Li, Z. Li, X.J. Loh, L. Song, E. Ye, Y. Xiong, Limiting the Uncoordinated N Species in M–N Single-Atom Catalysts toward Electrocatalytic CO_2 Reduction in Broad Voltage Range, Adv. Mater. 34(25) (2022) 2104090. https://doi.org/https://doi.org/10.1002/adma.202104090.
[22] X. Li, S.-G. Han, W. Wu, K. Zhang, B. Chen, S.-H. Zhou, D.-D. Ma, W. Wei, X.-T. Wu, R. Zou, Q.-L. Zhu, Convergent paired electrosynthesis of dimethyl carbonate from carbon dioxide enabled by designing the superstructure of axial oxygen coordinated nickel single-atom catalysts, Energy Environ. Sci. 16(2) (2023) 502-512. https://doi.org/10.1039/D2EE03022E.
[23] M. Huang, B. Deng, X. Zhao, Z. Zhang, F. Li, K. Li, Z. Cui, L. Kong, J. Lu, F. Dong, L. Zhang, P. Chen, Template-Sacrificing Synthesis of Well-Defined Asymmetrically Coordinated Single-Atom Catalysts for Highly Efficient CO_2 Electrocatalytic Reduction, ACS Nano 16(2) (2022) 2110-2119. https://doi.org/10.1021/acsnano.1c07746.
[24] X. Gu, Y. Jiao, B. Wei, T. Xu, P. Zhai, Y. Wei, J. Zuo, W. Liu, Q. Chen, Z. Yang, F. Zhao, X. Wang, L. Wang, Y. Gong, Boron bridged $NiN_4B_2C_x$ single-atom catalyst for superior electrochemical CO_2 reduction, Mater. Today 54 (2022) 63-71. https://doi.org/https://doi.org/10.1016/j.mattod.2022.02.008.
[25] Y. Guo, S. Yao, Y. Xue, X. Hu, H. Cui, Z. Zhou, Nickel single-atom catalysts intrinsically promoted by fast pyrolysis for selective electroreduction of CO_2 into CO, Appl. Catal. B: Environ. 304 (2022) 120997. https://doi.org/https://doi.org/10.1016/j.apcatb.2021.120997.
[26] S. Han, S. Jia, W. Xia, X. Xing, R. Qi, H. Wu, M. He, B. Han, A new strategy for mass production of single-atom catalysts for high performance of CO_2 electrochemical reduction, Chem. Eng. J. 455 (2023) 140595. https://doi.org/https://doi.org/10.1016/j.cej.2022.140595.
[27] L. Li, Z. Jiang, Y. Li, F. Li, Y. Pan, X. Zhang, Y. Liang, Z. Zheng, Regulating Morphological Features of Nickel Single-Atom Catalysts for Selective and Enhanced Electroreduction of CO_2, Small Methods 7(1) (2023) 2201213. https://doi.org/https://doi.org/10.1002/smtd.202201213.
[28] J. Wang, Y.-C. Huang, Y. Wang, H. Deng, Y. Shi, D. Wei, M. Li, C.-L. Dong, H. Jin, S.S. Mao, S. Shen, Atomically Dispersed Metal–Nitrogen–Carbon Catalysts with d-Orbital Electronic Configuration-Dependent Selectivity for Electrochemical CO_2-to-CO Reduction, ACS Catal. 13(4) (2023) 2374-2385. https://doi.org/10.1021/acscatal.2c05249.

[29] B. An, J. Zhou, L. Duan, X. Liu, G. Yu, T. Ren, X. Guo, Y. Li, H. Ågren, L. Wang, J. Zhang, Liquid Nitrogen Sources Assisting Gram-Scale Production of Single-Atom Catalysts for Electrochemical Carbon Dioxide Reduction, Adv. Sci. 10(11) (2023) 2205639. https://doi.org/https://doi.org/10.1002/advs.202205639.
[30] C. Lv, K. Huang, Y. Fan, J. Xu, C. Lian, H. Jiang, Y. Zhang, C. Ma, W. Qiao, J. Wang, L. Ling, Electrocatalytic reduction of carbon dioxide in confined microspace utilizing single nickel atom decorated nitrogen-doped carbon nanospheres, Nano Energy 111 (2023) 108384. https://doi.org/https://doi.org/10.1016/j.nanoen.2023.108384.
[31] H. Wang, Y. Li, M. Wang, S. Chen, M. Yao, J. Chen, X. Liao, Y. Zhang, X. Lu, E. Matios, J. Luo, W. Zhang, Z. Feng, J. Dong, Y. Liu, W. Li, Precursor-mediated in-situ growth of hierarchical N-doped graphene nanofibers confining nickel single atoms for CO_2 electroreduction, P. Natl. Acad. Sci. 120(14) (2023) e2219043120. https://doi.org/doi:10.1073/pnas.2219043120.
[32] T. Wang, J. Wang, C. Lu, K. Jiang, S. Yang, Z. Ren, J. Zhang, X. Liu, L. Chen, X. Zhuang, J. Fu, Single-Atom Anchored Curved Carbon Surface for Efficient CO_2 Electro-Reduction with Nearly 100% CO Selectivity and Industrially-Relevant Current Density, Adv. Mater. 35(35) (2023) 2205553. https://doi.org/https://doi.org/10.1002/adma.202205553.
[33] Z. Chen, C. Wang, X. Zhong, H. Lei, J. Li, Y. Ji, C. Liu, M. Ding, Y. Dai, X. Li, T. Zheng, Q. Jiang, H.-J. Peng, C. Xia, Achieving Efficient CO_2 Electrolysis to CO by Local Coordination Manipulation of Nickel Single-Atom Catalysts, Nano Lett. 23(15) (2023) 7046-7053. https://doi.org/10.1021/acs.nanolett.3c01808.
[34] J. Song, X. Lei, J. Mu, J. Li, X. Song, L. Yan, Y. Ding, Boron-Doped Nickel–Nitrogen–Carbon Single-Atom Catalyst for Boosting Electrochemical CO_2 Reduction, Small 19(52) (2023) 2305666. https://doi.org/https://doi.org/10.1002/smll.202305666.
[35] J. Song, X. Lei, J. Mu, J. Li, X. Song, L. Yan, Y. Ding, Chlorine-Coordinated Unsaturated Ni–N_2 Sites for Efficient Electrochemical Carbon Dioxide Reduction, Small 19(52) (2023) 2304423. https://doi.org/https://doi.org/10.1002/smll.202304423.
[36] X. Sun, L. Wang, X. Lan, Q. Lu, Y. Tuo, C. Ye, D. Wang, C. Xu, Positively charged nickel-sulfur dual sites for efficient CO_2 electroreduction reaction, Appl. Catal. B: Environ. 342 (2024) 123389. https://doi.org/https://doi.org/10.1016/j.apcatb.2023.123389.
[37] Z. Zeng, L.Y. Gan, H. Bin Yang, X. Su, J. Gao, W. Liu, H. Matsumoto, J. Gong, J. Zhang, W. Cai, Z. Zhang, Y. Yan, B. Liu, P. Chen, Orbital coupling of hetero-diatomic nickel-iron site for bifunctional electrocatalysis of CO_2 reduction and oxygen evolution, Nat. Commun. 12(1) (2021) 4088. https://doi.org/10.1038/s41467-021-24052-5.
[38] T. Zhang, X. Han, H. Liu, M. Biset-Peiró, X. Zhang, P. Tan, P. Tang, B. Yang, L. Zheng, J.R. Morante, J. Arbiol, Quasi-double-star nickel and iron active sites for high-efficiency carbon dioxide electroreduction, Energy Environ. Sci. 14(9) (2021) 4847-4857. https://doi.org/10.1039/D1EE01592C.
[39] L. Jiao, J. Zhu, Y. Zhang, W. Yang, S. Zhou, A. Li, C. Xie, X. Zheng, W. Zhou, S.-H. Yu, H.-L. Jiang, Non-Bonding Interaction of Neighboring Fe and Ni Single-Atom Pairs on MOF-Derived N-Doped Carbon for Enhanced CO_2 Electroreduction, J. Am. Chem. Soc. 143(46) (2021) 19417-19424. https://doi.org/10.1021/jacs.1c08050.
[40] D. Yao, C. Tang, X. Zhi, B. Johannessen, A. Slattery, S. Chern, S.-Z. Qiao, Inter-Metal Interaction with a Threshold Effect in NiCu Dual-Atom Catalysts for CO_2 Electroreduction, Adva. Mater. 35(11) (2023) 2209386. https://doi.org/https://doi.org/10.1002/adma.202209386.

[41] Z. Fan, R. Luo, Y. Zhang, B. Zhang, P. Zhai, Y. Zhang, C. Wang, J. Gao, W. Zhou, L. Sun, J. Hou, Oxygen-Bridged Indium-Nickel Atomic Pair as Dual-Metal Active Sites Enabling Synergistic Electrocatalytic CO_2 Reduction, Angew. Chem. Int. Ed. 62(7) (2023) e202216326. https://doi.org/https://doi.org/10.1002/anie.202216326.
[42] X.-M. Liang, H.-J. Wang, C. Zhang, D.-C. Zhong, T.-B. Lu, Controlled synthesis of a Ni_2 dual-atom catalyst for synergistic CO_2 electroreduction, Appl. Catal. B: Environ. 322 (2023) 122073. https://doi.org/https://doi.org/10.1016/j.apcatb.2022.122073.
[43] M. Wen, N. Sun, L. Jiao, S.-Q. Zang, H.-L. Jiang, Microwave-Assisted Rapid Synthesis of MOF-Based Single-Atom Ni Catalyst for CO_2 Electroreduction at Ampere-Level Current, Angew. Chemie Int. Ed. 63(10) (2024) e202318338. https://doi.org/https://doi.org/10.1002/anie.202318338.
[44] J.W. Lim, D.H. Choo, J.H. Cho, J. Kim, W.S. Cho, O.F. Ngome Okello, K. Kim, S. Lee, J. Son, S.-Y. Choi, J.K. Kim, H.W. Jang, S.Y. Kim, J.-L. Lee, A MOF-derived pyrrolic N-stabilized Ni single atom catalyst for selective electrochemical reduction of CO_2 to CO at high current density, J. Mater. Chem. A 12(18) (2024) 11090-11100. https://doi.org/10.1039/D3TA06399B.
[45] M. Liu, Y. Pang, B. Zhang, P. De Luna, O. Voznyy, J. Xu, X. Zheng, C.T. Dinh, F. Fan, C. Cao, F.P.G. de Arquer, T.S. Safaei, A. Mepham, A. Klinkova, E. Kumacheva, T. Filleter, D. Sinton, S.O. Kelley, E.H. Sargent, Enhanced electrocatalytic CO_2 reduction via field-induced reagent concentration, Nature 537(7620) (2016) 382-386. https://doi.org/10.1038/nature19060.
[46] H. Wang, Y. Fu, Z.-N. Chen, W. Zhuang, M. Cao, R. Cao, Tunable CO_2 enrichment on functionalized Au surface for enhanced CO_2 electroreduction, Nano Res. 16(4) (2023) 4723-4728. https://doi.org/10.1007/s12274-022-5159-8.